Applied Catalysis B: Environment and Energy 355 (2024) 124167

Contents lists available at ScienceDirect

Applied Catalysis B: Environment and Energy

journal homepage: www.elsevier.com/locate/apcatb

Regulating the d-band center of Cu nanoparticles for efficient photo-driven catalytic CO_2 reduction

Libo Wang [a], Shumin Zhang [b], Liuyang Zhang [a,*], Jiaguo Yu [a,*]

[a] Laboratory of Solar Fuel, Faculty of Materials Science and Chemistry, China University of Geosciences, 68 Jincheng Street, Wuhan 430078, China
[b] Hunan Key Laboratory of Applied Environmental Photocatalysis, Changsha University, Changsha, Hunan 410022, China

ARTICLE INFO

Keywords:
D-band center
Localized surface plasmon resonance
Light-to-heat conversion
Work function
Solar fuels

ABSTRACT

The conversion of CO_2 into solar fuels via photo-driven catalytic reduction presents a promising avenue toward achieving carbon neutrality. Herein, copper-based catalysts are prepared and explored for photo-driven photothermal CO_2 reduction reaction. The optimized catalyst exhibits a consistent CO production rate of 165.9 mmol g^{-1} h^{-1} and 100% CO selectivity at ambient pressure. We unveil the intricate adsorption dynamics at play: H_2 molecules predominantly interact with and activate at Cu sites, while CO_2 molecules preferentially adsorb and activate at interfacial sites within the composites. Furthermore, we elucidate how the positive shift of the d-band center (ε_d) for Cu 3*d* orbitals significantly enhances H_2 adsorption and activation. Crucially, the subsequent dissociation of H_2 molecules at Cu sites drives the efficient conversion of adsorbed CO_2 molecules at interfacial sites into CO. Overall, our findings not only advance the theoretical understanding but also offer practical insights for realizing photothermal catalytic CO_2 reduction reactions.

1. Introduction

The catalytic conversion of CO_2 into high-value chemicals or fuels represents a viable strategy for mitigating the energy crisis and greenhouse effect [1–6]. Among the array of catalytic pathways available, the selective conversion of CO_2 to CO via the reverse water gas shift (RWGS) reaction ($CO_2 + H_2 \rightarrow CO + H_2O$, $\triangle H_{298\ K} = 41.2$ kJ mol^{-1}) has garnered considerable attention [7–10]. However, traditional RWGS processes often rely on thermal catalysis, which demands harsh reaction conditions, including high pressures (> 3 MPa) and high temperatures (> 200 °C) [7–9]. Hence, the pursuit of catalytic systems that facilitate efficient CO_2 to CO conversion under milder conditions compared to thermal catalytic methods holds greater significance.

Recently, the photothermal catalytic CO_2 hydrogenation reaction system, driven by abundant and clean sunlight under ambient pressure and mild conditions, has emerged as a focal point of research [7,8,11–16]. Within this reaction system, the photo-to-heat conversion ability of the catalyst plays a crucial role, particularly in facilitating endothermic reactions like the RWGS process [7,8,11–14]. Thus, the development of catalysts proficient in this photo-to-heat conversion is imperative for enhancing the efficiency of the photothermal catalytic CO_2 hydrogenation reaction [7,8,11–14]. Among various catalysts explored, those based on metal nanoparticles exhibiting localized surface plasmon resonance (LSPR) effects have demonstrated notable advantages [17–24]. Upon illumination, the LSPR-induced hot charge carriers in metallic nanoparticles can substantially elevate the surface temperature of the catalyst, thereby accelerating reaction kinetics [17–22].

Apart from the photo-to-heat conversion ability of the catalyst, the adsorption capacity of reactant molecules on the catalyst surface is another crucial factor that influences the performance of the photothermal catalytic CO_2 reduction reaction in a gas-solid phase reaction system [13,25,26]. The strength of adsorption, particularly of transition metals with gas reactant molecules, correlates closely with the position of the d-band center (ε_d) [27–32]. Specifically, the higher the position of ε_d, the stronger the adsorption capacity; conversely, the weaker it is [27–32]. Therefore, regulating the ε_d of transition metals to modify the adsorption behavior of reactant molecules on its surface proves crucial for the catalytic reaction process [27–32].

The nanostructured pseudo-boehmite (α-AlOOH) has been studied extensively for various applications, including catalyst supports, adsorbents, and catalyst promoters [33–36]. Especially, α-AlOOH is rich in surface hydroxyl groups, which efficiently adsorb and capture CO_2 molecules. This feature makes it highly advantageous in gas-solid CO_2

* Corresponding authors.
E-mail addresses: zhangliuyang@cug.edu.cn (L. Zhang), yujiaguo93@cug.edu.cn (J. Yu).

https://doi.org/10.1016/j.apcatb.2024.124167
Received 26 March 2024; Received in revised form 3 May 2024; Accepted 5 May 2024
Available online 8 May 2024

catalytic reaction systems [35,36]. Herein, we introduce highly dispersed Cu nanoparticles supported on α′-AlOOH as catalysts for the photo-driven photothermal catalytic CO_2 reduction reaction. These catalysts harness excellent LSPR effects, enabling CO_2 reduction reaction to occur under Xe lamp irradiation at ambient pressure without external heating. The optimized catalyst exhibits excellent catalytic performance and a high photo-to-heat conversion temperature in the photo-driven photothermal CO_2 reduction reaction. Theoretical calculations indicate that the positive shift of ε_d for Cu *3d* orbitals effectively promotes H_2 adsorption and activation. Also, the rapid conversion of CO_2 molecules into CO products will be facilitated by the effective dissociation of H_2 molecules. Furthermore, comparative experiments demonstrate that the catalysts developed in this study outperform commercial counterparts, underscoring their promising practical applications.

2. Preparation

The samples were prepared via a coprecipitation method. Initially, 4.39 g of $Cu(NO_3)_2{\cdot}xH_2O$ and 1.48 g of $Al(NO_3)_3{\cdot}9\ H_2O$ were dissolved in 100 mL of deionized water and stirred at 90 °C for 30 mins. Next, 50 mL of 0.5 mol L^{-1} Na_2CO_3 solution was added, and the resulting mixture was stirred at 90 °C for 60 mins. Afterward, the mixture underwent centrifugation, followed by repeated washing with deionized water and ethanol, and vacuum drying for 10 hours at 60 °C. Subsequently, the dried mixture was calcined in air at 350 °C for 5 hours, followed by reduction at 300 °C for 2 hours in a 10 vol% H_2/Ar flow (20 mL min^{-1}). The resulting samples were designated as 80%Cu/α′-AlOOH, with "80%" indicating the theoretical weight percentage of Cu content in the sample. Typically, the material used for characterization tests was the 80%Cu/α′-AlOOH sample (denoted as Cu/AO), unless stated otherwise. For comparison, Cu nanoparticles and α′-AlOOH (denoted as AO) were synthesized under the same reaction conditions without the addition of $Al(NO_3)_3{\cdot}9\ H_2O$ and $Cu(NO_3)_2{\cdot}xH_2O$, respectively.

3. Results and discussion

3.1. Structural characterization of catalysts

The crystal phase structures of prepared samples were investigated by X-ray powder diffraction (XRD). As depicted in Fig. 1, the diffraction peaks of Cu and AO corresponded precisely with the characteristic crystal phases of metallic Cu (JCPDS No. 85–1326) and pseudoboehmite (α′-AlOOH) (JCPDS No. 83–2384) [33,34], respectively.

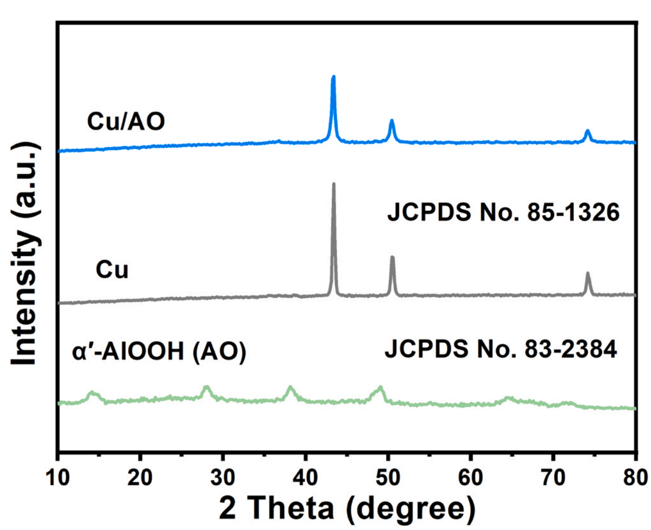

Fig. 1. XRD patterns of samples.

However, in the Cu/AO composite, no discernible diffraction peaks of AO are observed due to its relatively low diffraction intensity. Furthermore, the morphology and structural composition of the Cu/AO composite were further examined by transmission electron microscope (TEM) and high-resolution TEM. The TEM image (Fig. 2a) reveals a randomly aggregated layered structure within the Cu/AO composite. Correspondingly, the high-resolution TEM image showcases lattice fringes measuring 0.18 and 0.23 nm, which can be unequivocally indexed to the (200) plane of metallic Cu and the (031) plane of α′-AlOOH, respectively (Figs. 2b, 2c and 2d). In addition, the even distribution of O, Al, and Cu in the Cu/AO composite is aptly demonstrated by the corresponding high-angle annular dark field (HAADF) image (Fig. 2e) and EDS mapping images (Fig. 2f-h). These findings clearly corroborate the successful fabrication of Cu/AO composites, wherein metallic Cu nanoparticles are uniformly dispersed on the surface of AO support.

To identify the surface chemical states of samples, X-ray photoelectron spectroscopy (XPS) measurements were performed. As illustrated in Fig. 3a, the high-resolution Cu *2p* spectrum displayed doublet peaks at 932.9 and 952.7 eV, corresponding to the binding energies of Cu $2p_{3/2}$ and Cu $2p_{1/2}$ for metallic Cu^0, indicating the presence of supported Cu nanoparticles in the metallic state [37]. In Fig. 3b, the high-resolution O 1 s spectrum exhibited two distinct peaks: the peak at 530.2 eV was assigned to the lattice structure (Al-O bond), while the peak at 531.8 eV was attributed to the hydroxyl group of AO support [33,34]. Additionally, the peak at 74.1 eV was ascribed to the Al $2p_{3/2}$ peak (Fig. 3c) [19,34,37]. Notably, changes in the binding energy of the elements directly correlate with the gain and loss of electrons [38–41]. Furthermore, compared to the pristine Cu sample, the binding energies of Cu *2p* in Cu/AO composite significantly shift to higher binding energy regions, suggesting electron loss in Cu (Fig. 3a). Meanwhile, compared with the binding energy of O and Al in the pristine AO support, the peaks of O *1 s* and Al *2p* in the Cu/AO composite noticeably shift toward lower binding energy regions, implying an increase in the electron density of AO (Fig. 3b and 3c). Therefore, these XPS results suggest that electron transfer in the Cu/AO composite occurs from Cu nanoparticles to the AO support. Most importantly, the charge transfer behavior between Cu nanoparticles and AO support in the Cu/AO composite reveals the presence of strong metal-support interactions (SMSI), with electron transfer in composite materials often driven by differences in work functions between the components [38,39]. As shown in Fig. 3d and Fig. S1, the work function of AO (5.38 eV) is evidently larger than that of Cu (3.76 eV). Thereby, this finding provides critical evidence for SMSI and the electron transfer pathway from Cu nanoparticles to AO support in the Cu/AO composite. Additionally, the positively shifted binding energy of Cu *2p* spectrum, resulting from the SMSI effect, signifies the upshift of the d-band center (ε_d) of Cu *3d* orbitals, which is commonly regarded as an indicator of the high performance for catalytic reactions [31].

In addition, UV–vis diffuse reflectance spectra (UV–vis DRS) were analyzed to probe the light absorption capability and optical properties of samples, with relevant findings presented in Fig. 4a. Notably, the AO support exhibits limited absorption intensity across the 200–1400 nm range. In contrast, Cu nanoparticles display heightened light absorption intensity owing to their pronounced LSPR effect [17,20]. Most importantly, the light absorption intensity of the Cu/AO composite surpasses that of the Cu nanoparticles throughout the entire light absorption spectrum. This enhancement can be ascribed to the uniform dispersion of Cu nanoparticles achieved by incorporating the AO support, which effectively mitigates their aggregation. Besides, to assess the photothermal effect of the samples, surface temperature distributions were captured using a thermal imager camera under Xe lamp irradiation at an intensity of 3.8 W cm^{-2}. As illustrated in Fig. 4b, c and d, the maximum surface temperature of Cu/AO composite (474.9 °C) exceeds that of AO support (62.0 °C) and Cu nanoparticles (232.2 °C). This phenomenon confirms that the Cu/AO composite exhibits enhanced light-to-heat

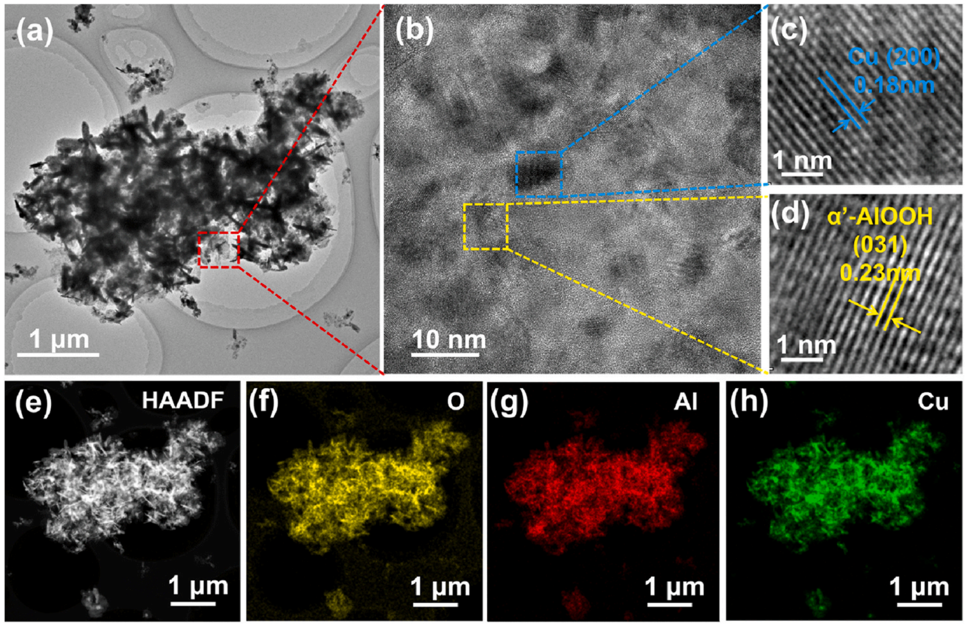

Fig. 2. (a) TEM image of Cu/AO. (b) HRTEM image of Cu/AO zooming into a region marked by the light blue and yellow dotted bordered rectangles, revealing lattice fringes of (c) Cu and (d) α'-AlOOH (AO), respectively. (e) High-angle annular dark-field (HAADF) image of Cu/AO. (f-h) EDS mapping images illustrating the distribution of O, Al, and Cu elements.

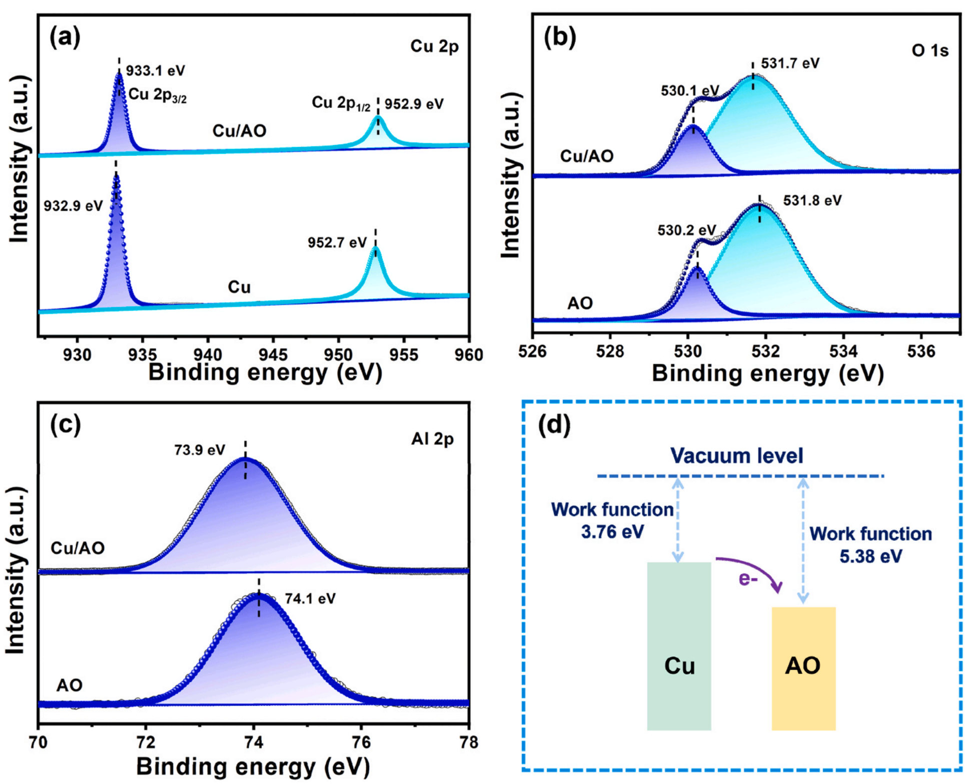

Fig. 3. (a) High-resolution XPS spectra of Cu *2p* of Cu and Cu/AO. High-resolution XPS spectra of (b) O *1 s* and (c) Al *2p* of AO and Cu/AO. (d) Schematic representation delineating the electron transfer mechanism between Cu and AO within the composite.

conversion, attributed to both the remarkable LSPR effect of Cu nanoparticles and their uniform dispersion on the surface of AO support. Additionally, photothermal conversion efficiency is a critical factor affecting the photothermal catalytic performance of CO_2 reduction [42]. Consequently, it is anticipated that the photothermal effect induced by light irradiation on the Cu/AO composite will bolster the performance of the CO_2 reduction reaction.

3.2. Catalytic performance of the samples

To evaluate the photothermal catalytic performance of samples, photothermal catalytic CO_2 hydrogenation experiments were conducted

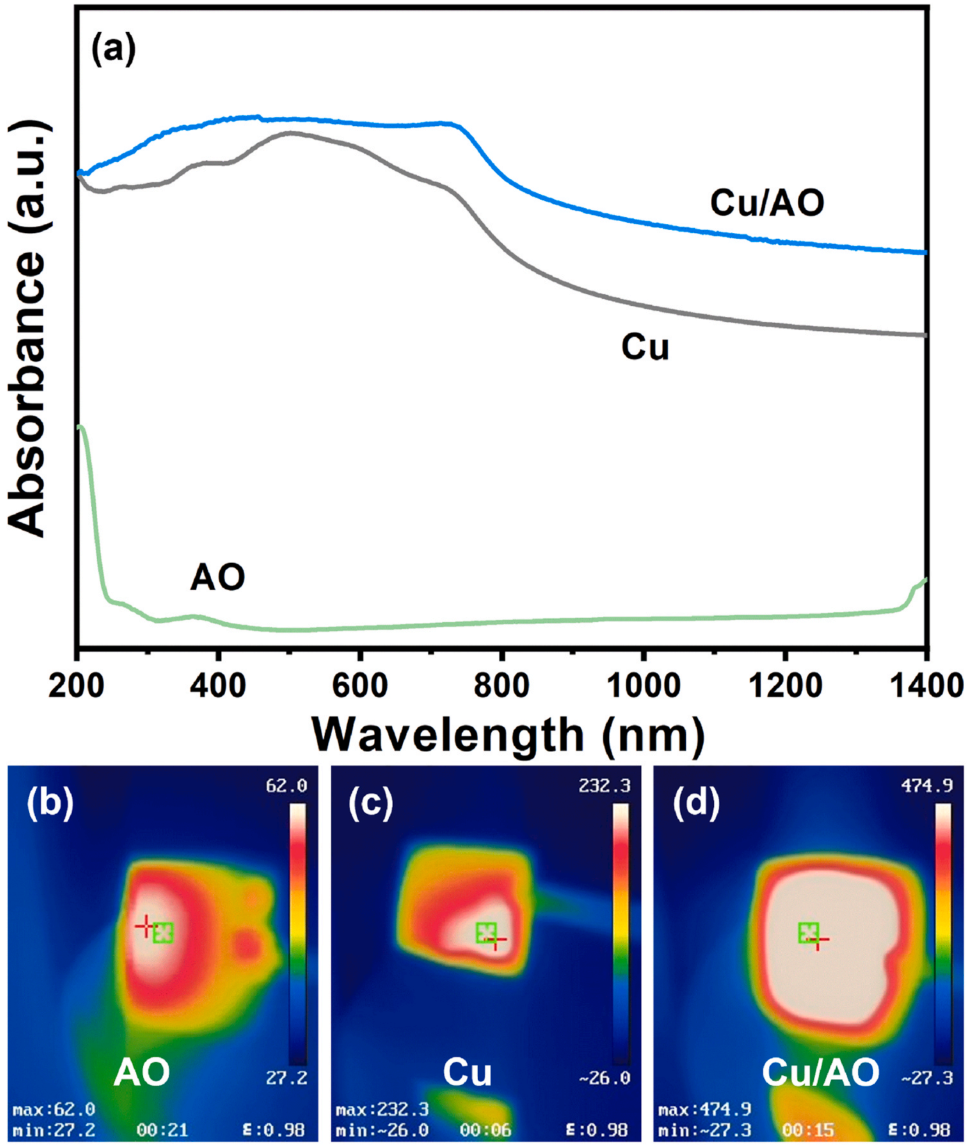

Fig. 4. (a) UV–vis DRS of samples. Thermal images captured under a Xe lamp light irradiation with an intensity of 3.8 W cm^{-2} for (b) AO, (c) pristine Cu, and (d) Cu/AO composite.

in a quartz batch reactor under Xe lamp irradiation (320 nm $< \lambda <$ 900 nm) at ambient pressure without any external heating (Fig. S2 and S3). As depicted in Fig. 5a, CO is the sole reduction product observed for all samples. Specifically, for Cu nanoparticles, the CO production rate is 22.1 mmol g^{-1} h^{-1}. Conversely, no products were detected on the pristine AO support, indicating its lack of photothermal catalytic CO_2 reaction activity. Importantly, the prepared x%Cu/AO composites exhibit significantly enhanced photothermal catalytic CO_2 reaction performance, with the CO production rate displaying a volcano trend as the Cu nanoparticle loadings increased. Of note, the optimum 80%Cu/AO (referred to as Cu/AO, the actual weight percentage of Cu is shown in Table S1) composite demonstrates the highest CO production rate of 165.9 mmol g^{-1} h^{-1}. Moreover, this photothermal catalytic CO_2 reduction performance is higher than many other photothermal catalysts under similar conditions (Table S2). Furthermore, to investigate the effects of light distribution in different regions on the CO production rate, a series of tests were carried out on the Cu/AO composite under 300 W Xe lamp with varying cut-off filters. As shown in Fig. S4, after the insertion of the cut-off filters ($\lambda >$ 400 nm and $\lambda >$ 500 nm), Cu/AO composite still has a high CO yield, suggesting that the photothermal CO_2 reduction reaction can be driven by visible and near-infrared light over Cu/AO composite. Additionally, for comparison, a sample of Cu-AO was prepared with the same Cu loading as Cu/AO composite through simple mixing. As depicted in Fig. S5, under identical reaction conditions, the CO production rate of Cu-AO (52.3 mmol g^{-1} h^{-1}) is lower than that of Cu/AO composite (165.9 mmol g^{-1} h^{-1}). This comparison highlights the significance of strong metal-support interactions in promoting the photothermal catalytic CO_2 reduction reaction.

Furthermore, the stability of the Cu/AO composite was assessed by repetitive photothermal catalytic CO_2 reduction reaction experiments conducted over five cycles. As shown in Fig. 5b, the consistent performance of photothermal catalytic CO_2 reduction over the five cycles indicates its superb stability. Furthermore, the XRD of the Cu/AO composite shows no noticeable change before and after the cyclic stability tests (Fig. S6). Simultaneously, the CO production rate of the Cu/AO composite is markedly higher than that of commercial thermal catalysts (comm-CuZnAl) (133.5 mmol g^{-1} h^{-1}) (Fig. S5), indicating the potential of Cu/AO composite for practical application.

Furthermore, to investigate the carbon origin of photothermal catalytic CO_2 reduction reaction products, a series of comparative experiments were performed under different reaction conditions. As depicted in Fig. S7, the absence of either light or the Cu/AO composite resulted in

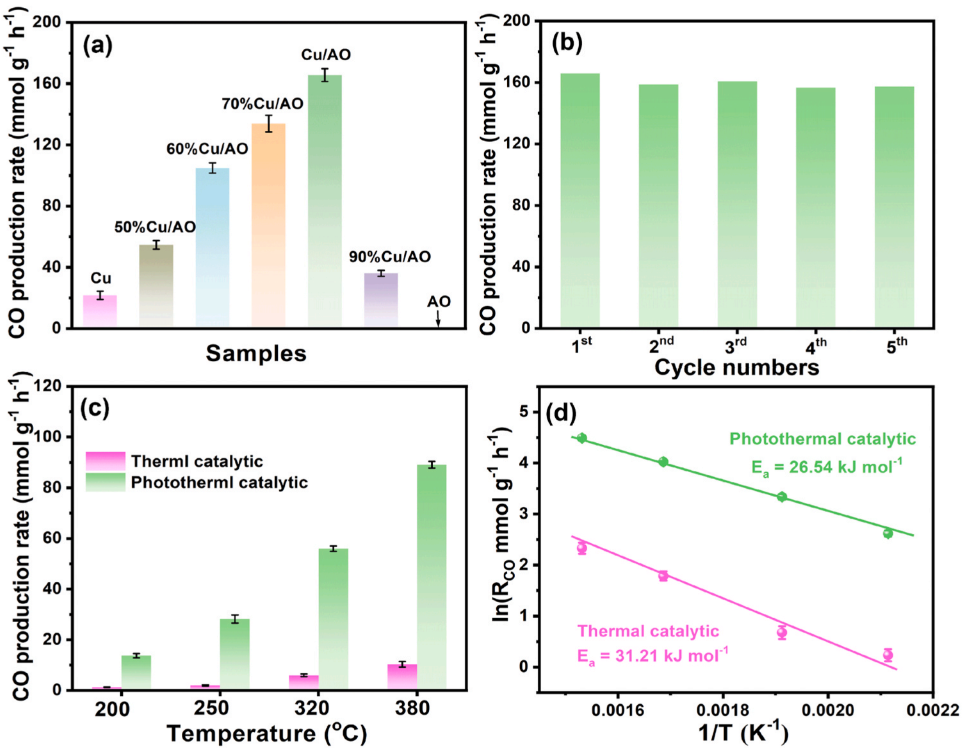

Fig. 5. (a) Photothermal catalytic performance evaluation of samples under a 3.8 W cm^{-2} light intensity illumination without external heating. (b) Stability assessment of Cu/AO composite under a 3.8 W cm^{-2} light intensity illumination without external heating. (c) Comparative analysis of photothermal catalytic and thermal catalytic CO_2 reduction over Cu/AO composite, and (d) the corresponding Arrhenius plot.

no observable CO product, implying that the photothermal catalytic CO_2 reduction reaction is a light-induced catalytic reaction on the Cu/AO composite. Notably, when the reaction was conducted without H_2 gas, no reaction products were detected, indicating the importance of H_2 as a reactant in the photothermal catalytic CO_2 reduction reaction. Besides, no reaction products were detected when Ar gas was used instead of CO_2 or H_2/CO_2 gas mixture, providing direct evidence that the photothermal catalytic CO_2 reduction reaction products (CO) originate from the fed CO_2 rather than from adventitious carbon sources.

Additionally, in the light-induced photothermal catalytic reaction system, the dispersion confinement effect of the AO support for the Cu nanoparticles aids in ensuring that the heat generated by the Cu nanoparticles via the LSPR effect is confined around the catalytic active sites. This confinement effectively prevents heat diffusion throughout the entire reaction system, minimizing heat loss and thereby improving the catalytic reaction rate on the surface of Cu/AO composite [43,44]. Meanwhile, under irradiation, Cu nanoparticles produce hot carriers with significantly higher energy levels than those generated by thermal excitation. These energetic hot carriers can migrate to unoccupied molecular orbitals of adsorbate molecules, initiating photochemical reactions that differ from the traditional thermal pathways [43,44].

To further investigate the impact of light irradiation on the photothermal catalytic CO_2 reduction performance of Cu/AO composite, experiments were conducted comparing photo-induced photothermal catalytic without external heating and thermal catalytic without light irradiation at the same temperature. The surface temperature of the Cu/AO composite is regulated by adjusting the current intensity of the Xe lamp under illuminated conditions (Fig. S8), whereas an auxiliary heat source controls the reaction temperature under dark conditions. Although the CO production rate increased with increasing temperature of the reaction system due to the endothermic nature of the RWGS reaction, the overall performance of the photothermal catalytic over Cu/AO composite is significantly higher than that of the thermal catalytic without light irradiation (Fig. 5c), indicating that the light irradiation can effectively enhance the activity of RWGS reaction. Meanwhile, to gain further insights into the higher performance of light-induced RGWS reaction, the apparent activation energy (E_a) of photothermal catalytic and thermal catalytic reactions were calculated according to the Arrhenius plot, respectively. As shown in Fig. 5d, the E_a of the photothermal catalytic reaction (24.64 kJ mol^{-1}) is obviously lower than that of the thermal catalytic reaction (30.91 kJ mol^{-1}), manifesting that the light irradiation effectively reduced the E_a of RWGS reaction, which is beneficial for the formation of reduction products [45–47].

3.3. Mechanisms of photothermal catalytic CO_2 reduction reaction

The influence of reactant adsorption on the catalyst surface is paramount in shaping the performance of the photothermal catalytic CO_2 reduction reaction in gas-solid phase reaction systems. Meanwhile, to evaluate the physical properties of samples, N_2 adsorption-desorption and CO_2 adsorption isotherms were measured, respectively. As shown in Fig. 6a, the N_2 adsorption-desorption isotherms exhibit a type IV physisorption isotherm with noticeable hysteresis for the AO support, implying characteristic mesopores. Brunauer-Emmett-Teller (BET) surface area (S_{BET}) and pore volume of Cu/AO composite are noticeably higher at 27 m^2 g^{-1} and 0.44 cm^3 g^{-1}, respectively, compared to Cu nanoparticles (1.5 m^2 g^{-1}, 0.03 cm^3 g^{-1}) (Table S3). Correspondingly, the CO_2 adsorption capacity of Cu/AO composite (0.46 mmol g^{-1}) is superior to that of Cu nanoparticles (0.21 mmol g^{-1}) (Fig. 6b). These results indicate that the introduction of AO support dramatically increases the S_{BET}, pore volume and CO_2 adsorption capacity of samples.

Besides, CO_2 temperature programmed desorption (CO_2-TPD) experiments of samples were performed, with results shown in Fig. 6c. All samples exhibit peaks at 100 °C, which is ascribed to the physically adsorbed CO_2 molecules [13,14,37,48]. Interestingly, no such peak was detected for Cu nanoparticles apart from those in the low-temperature region, indicating their inefficacy in capturing and adsorbing CO_2 molecules [13,14,37,48]. By contrast, both the AO support and Cu/AO

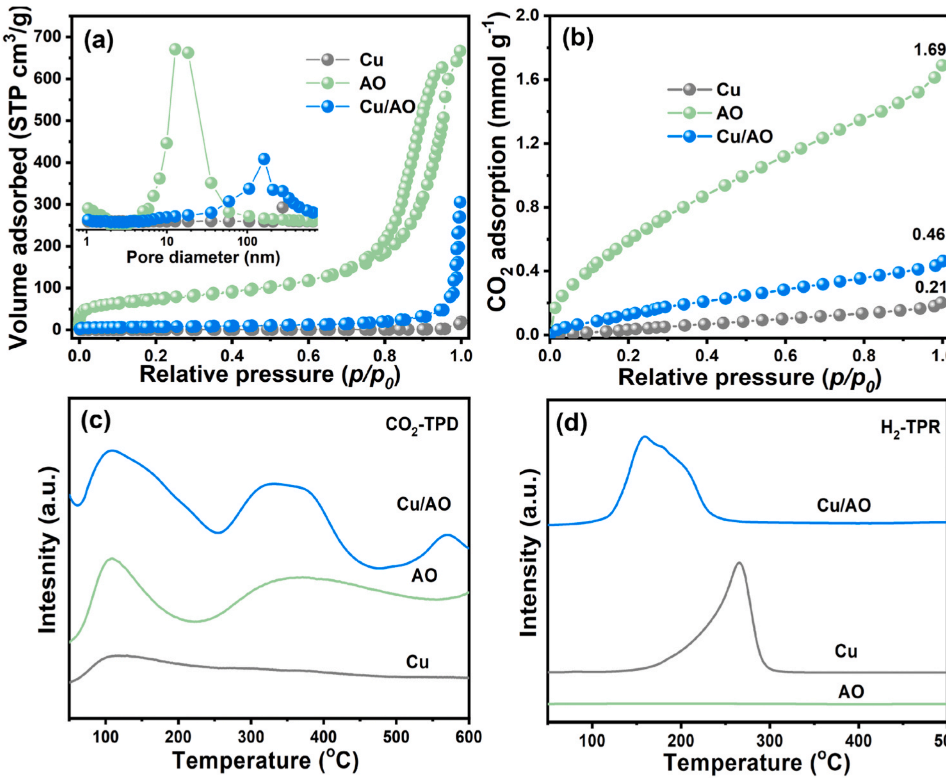

Fig. 6. (a) N_2 adsorption-desorption isotherms and pore distribution curves, (b) CO_2 adsorption isotherms, (c) CO_2-TPD, and (d) H_2-TPR profiles of samples.

composites displayed a broad and prominent desorption peak in the 300–400 °C range, indicative of chemically bonded CO_2 molecules on the sample surface [13,14,37,48]. This chemical adsorption of CO_2 molecules is associated with the -OH functional groups acting as basicity sites on the surface of AO support [14]. Notably, compared to the AO support and Cu nanoparticles, a distinct CO_2 desorption peak around 570 °C was observed for the curve of Cu/AO composites, attributed to the desorption of strongly chemosorbed CO_2 molecules at the interface between AO support and Cu nanoparticles. This suggests that the interface sites are vital in enhancing the CO_2 adsorption capacity [13]. Furthermore, to investigate the H_2 dissociation behavior of samples, H_2 temperature programmed reduction (H_2-TPR) experiments were performed. As shown in Fig. 6d, the absence of a peak in the curve of AO support indicates its inertness in the H_2 atmosphere and inability to split H_2 molecules. Conversely, a strong peak at around 270 °C was detected for the Cu nanoparticles, indicating the robust H_2 splitting ability. Remarkably, compared with the Cu nanoparticles, the peak in Cu/AO composite shifts to a lower temperature, suggesting easier dissociation of H_2 molecules [13]. These results suggest that the introduction of AO support to disperse Cu nanoparticles can effectively promote the dissociation of H_2 molecules, and the interfacial sites formed by the contact between AO support and Cu nanoparticles can effectively enhance CO_2 adsorption.

To delve deeper into the sites involved in the adsorption of H_2 and CO_2 molecules on the Cu/AO composite, density functional theory (DFT) calculations were conducted. Fig. 7a-h illustrate the optimized H_2 and CO_2 molecule adsorption structures on various adsorption sites. The theoretical results disclose that the adsorption energy (E_{ads}) of H_2 molecule on the surface of Cu nanoparticles (-0.56 eV, Fig. 7a) is significantly negative compared to the E_{ads} of CO_2 molecule (-0.18 eV, Fig. 7e), indicating facile adsorption of H_2 molecule on the surface of Cu nanoparticles. In contrast, the E_{ads} of H_2 molecule on AO support (-0.06 eV, Fig. 7b) is considerably more positive than that of the CO_2 molecule (-0.25 eV, Fig. 7f), implying preferential adsorption of CO_2 on the surface of AO support. Notably, compared to the adsorption energy (E_{ads}) of H_2 molecule on Cu nanoparticles (Fig. 7a), AO support (Fig. 7b), and the interface of Cu/AO composite (Fig. 7d), the E_{ads} of H_2 molecule on the Cu surface of Cu/AO composite is the most negative (-0.91 eV, Fig. 7c), with the H-H bond length of H_2 molecule being the longest (0.83 Å), indicating enhanced adsorption and activation of H_2 molecule on the Cu site of Cu/AO composite [13]. In addition, compared to the E_{ads} of CO_2 molecule on the various sites, the interfacial site of Cu/AO composite exhibits the maximum E_{ads} of CO_2 molecule (-0.48 eV, Fig. 7h), underlining the essential role of heterogeneous interfaces in CO_2 adsorption. Furthermore, the C-O bond length and the C-O-C bond angle of CO_2 on the surface of Cu nanoparticles are compared, indicating efficient activation of chemically inert CO_2 at the interfacial site of Cu/AO composite (Fig. 7e-h) [13,49]. Thus, based on these theoretical results in conjunction with the above H_2-TPR and CO_2-TPD results, it can be inferred that the Cu component within the Cu/AO composite serves as the adsorption active site for H_2 molecules. At the same time, the heterogeneous interface acts as the adsorption active site for CO_2 molecules.

Additionally, the ε_d of Cu nanoparticles and Cu/AO composite were calculated from the partial density of states of Cu *3d* orbitals. As shown in Fig. 7i and j, the ε_d of Cu in the Cu/AO composite (-1.43 eV) is significantly more positive than that of Cu nanoparticles (-1.61 eV), stating an upward shift of ε_d for Cu after the formation of Cu/AO composite. This result aligns with the conclusion of the XPS experiment. In accordance with the d-band theory, as the proximity of ε_d to the Fermi level increases, so does the strength of the bond formed between the active site and the adsorbate [27–32]. Most notably, the upward shift of the ε_d for the Cu nanoparticles has a greater impact on H_2 adsorption compared to CO_2, as it serves as the primary adsorption active site for the H_2 molecule. Hence, based on the obtained results, a schematic diagram of the adsorption and activation of H_2 molecule on the surface of Cu/AO composite is provided in Fig. 7k. When H_2 molecules chemically adsorb onto the surface of Cu nanoparticles, hybridization occurs between the d orbitals of Cu and the σ molecular orbitals of H_2, resulting in the formation of d-σ bonding and d-σ anti-bonding states [50]. The d-σ

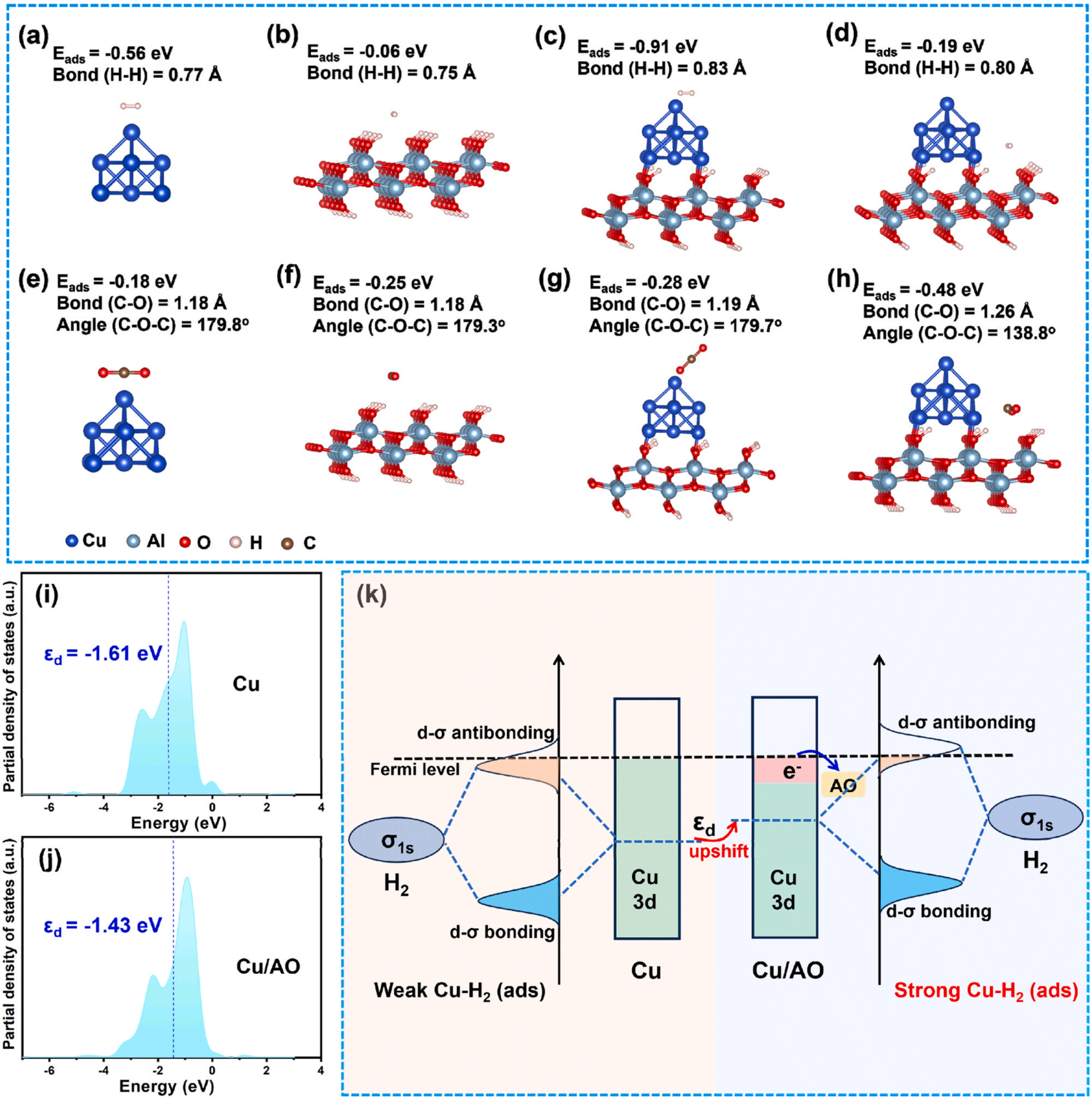

Fig. 7. Optimized structures of H_2 molecule adsorption on (a) the surface of Cu nanoparticles, (b) the surface of AO support, (c) the surface of Cu in Cu/AO composite, and (d) the interface of Cu/AO composite. Optimized structures of CO_2 molecule adsorbed on (e) the surface of Cu nanoparticles, (f) the surface of AO support, (g) the surface of Cu in Cu/AO composite, and (h) the interface of Cu/AO composite. Cu, Al, O, H, and C atoms are presented with blue, silver, red, pink, and brown balls, respectively. Partial density of states for d orbitals of (i) Cu and (j) Cu in Cu/AO composite. The d-band center (ε_d) is indicated by a blue dotted line. (k) Schematic illustration of weak (left) and strong (right) d-σ orbital hybridization for Cu-H_2.

bonding states are occupied, while the d-σ anti-bonding states are partially occupied. After the formation of the Cu/AO composite, the d-band electrons of Cu are transferred to the AO support due to differences in work functions, resulting in a significant upshift of ε_d for Cu. In this scenario, the ε_d is in proximity to the Fermi level, with the energy of the anti-bonding state higher than that of the Fermi level, effectively reducing the degree of occupied anti-bonding state and promoting strong chemical interactions between Cu and H_2 molecules, thereby enhancing H_2 activation.

To explore the active sites crucial for the adsorption of H_2 and CO_2 molecules on the Cu/AO composite, the *in-situ* DRIFTS were performed. As shown in Fig. 8a, peaks located at 3607, 3628, 3704, and 3727 cm^{-1} correspond to the characteristic peaks of gaseous CO_2, suggesting the efficient CO_2 adsorption on the Cu/AO composites even without light irradiation [13,47,48,51]. Furthermore, new peaks emerge in the DRIFTS spectra under irradiation conditions. The broad peak that appears at 1241 cm^{-1} can be assigned to the COOH* species, which are the essential intermediates in the CO_2 reduction process [13,47,48,51]. Strong peaks at 1634 and 3320 cm^{-1} are attributed to the typical vibrational modes of H_2O and -OH groups, respectively [13,47,48,51]. Additionally, the presence of gaseous CO (2137 cm^{-1}) can be detected [51]. These new peaks unequivocally indicate the successful conversion of the CO_2 and H_2 to CO and H_2O on the Cu/AO composite surface. Therefore, according to the *in-situ* DRIFTS, DFT, H_2-TPR, and CO_2-TPD analyses, a plausible photothermal catalysis CO_2 reduction reaction conversion pathway over Cu/AO composites can be proposed (Fig. 8b).

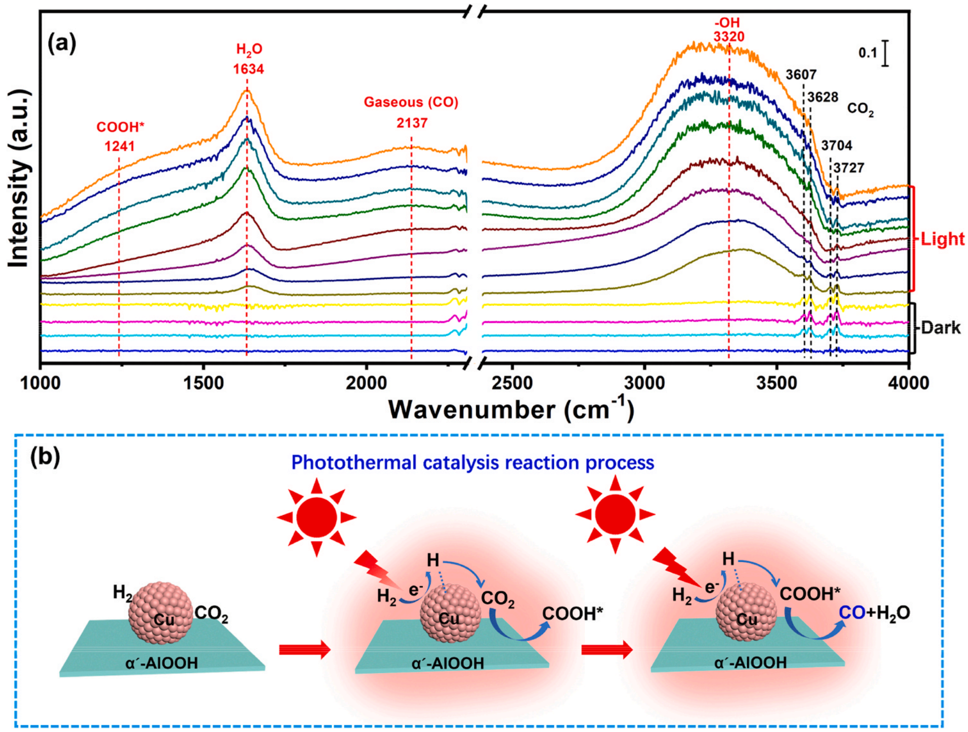

Fig. 8. (a) *In-situ* diffuse reflectance infrared Fourier transform spectroscopy (DRIFTS) of Cu/AO composites measured under dark and light irradiation conditions in a CO_2/H_2 (50/50 vol%) mixture atmosphere. (b) Schematic illustration of photothermal catalysis reaction process over Cu/AO composites.

Upon introducing CO_2 and H_2 mixed gas into the reaction system, CO_2 molecules are adsorbed on the interfacial sites of Cu/AO composite. In contrast, H_2 molecules are adsorbed on the Cu surface of Cu/AO composite. Under light irradiation, high temperatures are generated on the Cu/AO composite surface due to the excellent LSPR effect of Cu nanoparticles. Concurrently, photoinduced hot electrons from Cu nanoparticles are transferred to the adsorbed H_2 molecules through strong d-σ orbital hybridization of Cu-H_2, facilitating the dissociation of H_2 molecules into active H radicals [13,52]. As active H radicals accumulate at the Cu sites, a large number of them spill over from Cu sites to the interfacial sites between Cu and AO support, reacting with CO_2 molecules adsorbed at the interfacial sites to form COOH* species. Ultimately, COOH* species react with active H radicals to form CO and H_2O, completing the reduction and conversion of CO_2 to CO.

4. Conclusions

In conclusion, our synthesis of the Cu/AO composite has yielded a material with remarkable light-to-heat conversion capabilities and outstanding performance in catalyzing the photo-induced reduction of CO_2. The optimized Cu/AO composite demonstrates exceptional selectivity, producing CO exclusively, and achieves an impressive CO production rate of 165.9 mmol g^{-1} h^{-1} under Xe lamp irradiation at ambient pressure without requiring external heating. Through a combination of experimental characterizations and DFT calculations, we have elucidated that CO_2 molecules predominantly adsorb and activate at the interfacial sites of the Cu/AO composite, while H_2 molecules primarily adsorb and activate at the Cu surface of the composite. This enhanced catalytic activity is attributed to the effective dissociation of H_2 molecules on the surface of Cu nanoparticles, facilitated by the positive shift of the Cu *3d* orbital energy levels (ε_d) due to the different work functions between the Cu nanoparticles and the AO support. Our findings suggest a promising strategy for harnessing solar energy to drive the efficient conversion of CO_2 into valuable solar fuels, highlighting the potential impact of our work on advancing sustainable energy technologies.

CRediT authorship contribution statement

Libo Wang: Writing – original draft, Software, Investigation, Formal analysis, Data curation, Conceptualization. **Shumin Zhang:** Validation, Data curation. **Liuyang Zhang:** Writing – review & editing, Funding acquisition, Formal analysis, Conceptualization. **Jiaguo Yu:** Supervision, Resources, Project administration, Funding acquisition, Formal analysis, Conceptualization.

Declaration of Competing Interest

The authors declare that they have no known competing financial interests or personal relationships that could have appeared to influence the work reported in this paper.

Data Availability

Data will be made available on request.

Acknowledgments

This work was supported by the National Key Research and Development Program of China (2022YFB3803600 and 2022YFE0115900), the National Natural Science Foundation of China (NSFC) (52202376, 22361142704, 22238009, 51932007, 22278383), the Natural Science Foundation of Hubei Province of China (2022CFA001) and the China Postdoctoral Science Foundation (2022TQ0316).

Appendix A. Supporting information

Supplementary data associated with this article can be found in the online version at doi:10.1016/j.apcatb.2024.124167.

References

[1] A. Velty, A. Corma, Advanced zeolite and ordered mesoporous silica-based catalysts for the conversion of CO_2 to chemicals and fuels, Chem. Soc. Rev. 52 (2023) 1773–1946.

[2] H. Li, Y. Chen, Q. Niu, X. Wang, Z. Liu, J. Bi, Y. Yu, L. Li, The crystalline linear polyimide with oriented photogenerated electron delivery powering CO_2 reduction, Chin. J. Catal. 49 (2023) 152–159.

[3] J. Zhang, J. Fu, K. Dai, Graphitic carbon nitride/antimonene van der Waals heterostructure with enhanced photocatalytic CO_2 reduction activity, J. Mater. Sci. Technol. 116 (2022) 192–198.

[4] M. Lin, M. Luo, Y. Liu, J. Shen, J. Long, Z. Zhang, 1D S-scheme heterojunction of urchin-like SiC-$W_{18}O_{49}$ for enhancing photocatalytic CO_2 reduction, Chin. J. Catal. 50 (2023) 239–248.

[5] W. Jiang, H. Loh, B. Low, H. Zhu, J. Low, J. Heng, K.Y. Tang, Z. Li, X. Loh, E. Ye, Role of oxygen vacancy in metal oxides for photocatalytic CO_2 reduction, Appl. Catal. B: Environ. 321 (2023) 122079.

[6] Z. Zhong, H. Wang, S. Liang, X. Zhong, H. Deng, Enhancing photocatalytic CO_2 reduction reaction on amorphous Ni@NiO aerogel via oxygen incorporated tuning, Appl. Catal. B: Environ. 330 (2023) 122603.

[7] G. Chen, G. Waterhouse, R. Shi, J. Zhao, Z. Li, L.Z. Wu, C. Tung, T. Zhang, From solar energy to fuels: recent advances in light-driven C1 chemistry, Angew. Chem. Int. Ed. 58 (2019) 17528–17551.

[8] J. Ma, J. Yu, G. Chen, Y. Bai, S. Liu, Y. Hu, M. Al-Mamun, Y. Wang, W. Gong, D. Liu, Rational design of N-doped carbon-coated cobalt nanoparticles for highly efficient and durable photothermal CO_2 conversion, Adv. Mater. 35 (2023) 2302537.

[9] J. Graciani, K. Mudiyanselage, F. Xu, A. Baber, J. Evans, S. Senanayake, D. Stacchiola, P. Liu, J. Hrbek, J. Sanz, Highly active copper-ceria and copper-ceria-titania catalysts for methanol synthesis from CO_2, Science 345 (2014) 546–550.

[10] B. Deng, H. Song, K. Peng, Q. Li, J. Ye, Metal-organic framework-derived Ga-Cu/CeO_2 catalyst for highly efficient photothermal catalytic CO_2 reduction, Appl. Catal. B: Environ. 298 (2021) 120519.

[11] M. Cai, Z. Wu, Z. Li, L. Wang, W. Sun, A. Tountas, C. Li, S. Wang, K. Feng, A. Xu, Greenhouse-inspired supra-photothermal CO_2 catalysis, Nat. Energy 6 (2021) 807–814.

[12] C. Lv, X. Bai, S. Ning, C. Song, Q. Guan, B. Liu, Y. Li, J. Ye, Nanostructured materials for photothermal carbon dioxide hydrogenation: regulating solar utilization and catalytic performance, ACS Nano 17 (2023) 1725–1738.

[13] C. Guo, Y. Tang, Z. Yang, T. Zhao, J. Liu, Y. Zhao, F. Wang, Reinforcing the efficiency of photothermal catalytic CO_2 methanation through Integration of Ru nanoparticles with photothermal $MnCo_2O_4$ nanosheets, ACS Nano 17 (2023) 23761–23771.

[14] H. Wang, Q. Li, J. Chen, J. Chen, H. Jia, Efficient solar-driven CO_2 methanation and hydrogen storage over nickel catalyst derived from metal-organic frameworks with rich oxygen vacancies, Adv. Sci. 10 (2023) 2304406.

[15] B. Deng, H. Song, Q. Wang, J. Hong, S. Song, Y. Zhang, K. Peng, H. Zhang, T. Kako, J. Ye, Highly efficient and stable photothermal catalytic CO_2 hydrogenation to methanol over Ru/In_2O_3 under atmospheric pressure, Appl. Catal. B: Environ. 327 (2023) 122471.

[16] K. Peng, J. Ye, H. Wang, H. Song, B. Deng, S. Song, Y. Wang, L. Zuo, J. Ye, Natural halloysite nanotubes supported Ru as highly active catalyst for photothermal catalytic CO_2 reduction, Appl. Catal. B: Environ. 324 (2023) 122262.

[17] M. Sayed, J. Yu, G. Liu, M. Jaroniec, Non-noble plasmonic metal-based photocatalysts, Chem. Rev. 122 (2022) 10484–10537.

[18] R. Ciocarlan, N. Blommaerts, S. Lenaerts, P. Cool, S. Verbruggen, Recent trends in plasmon-assisted photocatalytic CO_2 reduction, ChemSusChem 16 (2023) e202201647.

[19] Y. Kim, D. Wi, J. Hong, S. Han, Plasmonic nanocrystal assembly–semiconductor hybrids for boosting visible to near-infrared photocatalysis, ACS Nano 17 (2023) 18641–18651.

[20] S. Linic, P. Christopher, D. Ingram, Plasmonic-metal nanostructures for efficient conversion of solar to chemical energy, Nat. Mater. 10 (2011) 911–921.

[21] A. Cheruvathoor Poulose, G. Zoppellaro, I. Konidakis, E. Serpetzoglou, E. Stratakis, O. Tomanec, M. Beller, A. Bakandritsos, R. Zbořil, Fast and selective reduction of nitroarenes under visible light with an earth-abundant plasmonic photocatalyst, Nat. Nanotechnol. 17 (2022) 485–492.

[22] Y. Li, J. Hao, H. Song, F. Zhang, X. Bai, X. Meng, H. Zhang, S. Wang, Y. Hu, J. Ye, Selective light absorber-assisted single nickel atom catalysts for ambient sunlight-driven CO_2 methanation, Nat. Commun. 10 (2019) 2359.

[23] Y. Zhang, M. Gao, S. Chen, H. Wang, P. Huo, Fabricating Ag/CN/$ZnIn_2S_4$ S-scheme heterojunctions with plasmonic effect for enhanced light-driven photocatalytic CO_2 reduction, Acta Phys. -Chim. Sin. 39 (2023) 2211051.

[24] H. He, Z. Wang, K. Dai, S. Li, J. Zhang, LSPR-enhanced carbon-coated In_2O_3/$W_{18}O_{49}$ S-scheme heterojunction for efficient CO_2 photoreduction, Chin. J. Catal. 48 (2023) 267–278.

[25] C. Luo, Q. Long, B. Cheng, B. Zhu, L. Wang, A DFT study on S-scheme heterojunction consisting of Pt single atom loaded g-C_3N_4 and BiOCl for photocatalytic CO_2 reduction, Acta Phys. -Chim. Sin. 39 (2023) 2212026.

[26] F. Xie, C. Bie, J. Sun, Z. Zhang, B. Zhu, A DFT study on Pt single atom loaded COF for efficient photocatalytic CO_2 reduction, J. Mater. Sci. Technol. 170 (2024) 87–94.

[27] Z. Li, Z. Tian, H. Cheng, T. Wang, W. Zhang, Y. Lu, Y. Lai, G. He, Engineering d-band center of FeN_4 moieties for efficient oxygen reduction reaction electrocatalysts, Energy Storage Mater. 59 (2023) 102764.

[28] Z. Ma, X. Liu, X. Wang, Z. Luo, W. Li, Y. Nie, L. Pei, Q. Mao, X. Wen, J. Zhong, Manipulating the d-band center enhances photoreduction of CO_2 to CO in Zn_2GeO_4 nanorods, Chem. Eng. J. 468 (2023) 143569.

[29] X. Sun, L. Sun, G. Li, Y. Tuo, C. Ye, J. Yang, J. Low, X. Yu, J. Bitter, Y. Lei, Phosphorus tailors the d-band center of copper atomic sites for efficient CO_2 photoreduction under visible-light irradiation, Angew. Chem. Int. Ed. 61 (2022) e202207677.

[30] S. Joo, K. Kim, O. Kwon, J. Oh, H.J. Kim, L. Zhang, J. Zhou, J.Q. Wang, H.Y. Jeong, J.W. Han, Enhancing thermocatalytic activities by upshifting the d-band center of exsolved Co-Ni-Fe ternary alloy nanoparticles for the dry reforming of methane, Angew. Chem. Int. Ed. 60 (2021) 15912–15919.

[31] P. Kuang, Z. Ni, B. Zhu, Y. Lin, J. Yu, Modulating the d-band center enables ultrafine Pt_3Fe alloy nanoparticles for pH-universal hydrogen evolution reaction, Adv. Mater. 35 (2023) 2303030.

[32] J. Wang, Y. Zhang, S. Jiang, C. Sun, S. Song, Regulation of d-band centers in localized CdS homojunctions through facet control for improved photocatalytic water splitting, Angew. Chem. Int. Ed. 135 (2023) e202307808.

[33] S. Liu, M. Dong, Y. Wu, S. Luan, Y. Xin, J. Du, S. Li, H. Liu, B. Han, Solid surface frustrated Lewis pair constructed on layered AlOOH for hydrogenation reaction, Nat. Commun. 13 (2022) 2320.

[34] Z. Yan, Z. Xu, J. Yu, M. Jaroniec, Effect of microstructure and surface hydroxyls on the catalytic activity of Au/AlOOH for formaldehyde removal at room temperature, J. Colloid Interface Sci. 501 (2017) 164–174.

[35] C. Jiang, M. Fan, G. Gao, W. Jiang, X. Li, C. Luo, L. Zhang, F. Wu, Nanostructured AlOOH-A promising catalyst to reduce energy consumption for amine-based CO_2 capture, Sep. Purif. Technol. 303 (2022) 122232.

[36] Y. Chang, Y. Chen, P. Chang, S. Chen, Synthesis, characterization, and CO_2 adsorptive behavior of mesoporous AlOOH-supported layered hydroxides, ChemSusChem 5 (2012) 1249–1257.

[37] X. Song, C. Yang, X. Li, Z. Wang, C. Pei, Z. Zhao, J. Gong, On the role of hydroxyl groups on Cu/Al_2O_3 in CO_2 hydrogenation, ACS Catal. 12 (2022) 14162–14172.

[38] J. Zhang, L. Zhang, W. Wang, J. Yu, In situ irradiated X-ray photoelectron spectroscopy investigation on electron transfer mechanism in S-scheme photocatalyst, J. Phys. Chem. Lett. 13 (2022) 8462–8469.

[39] L. Wang, B. Cheng, L. Zhang, J. Yu, In situ irradiated XPS investigation on S-scheme TiO_2@$ZnIn_2S_4$ photocatalyst for efficient photocatalytic CO_2 reduction, Small 17 (2021) 2103447.

[40] J. Wang, X. Qiao, W. Shi, J. He, J. Chen, W. Zhang, S-scheme heterojunction of Cu_2O polytope-modified BiOI sheet for efficient visible-light-driven CO_2 conversion under water vapor, Acta Phys. -Chim. Sin. 39 (2023) 2210003.

[41] L. Wang, X. Fei, L. Zhang, J. Yu, B. Cheng, Y. Ma, Solar fuel generation over nature-inspired recyclable TiO_2/g-C_3N_4 S-scheme hierarchical thin-film photocatalyst, J. Mater. Sci. Technol. 112 (2022) 1–10.

[42] L. Wang, H. Tan, L. Zhang, B. Cheng, J. Yu, In-situ growth of few-layer graphene on ZnO with intimate interfacial contact for enhanced photocatalytic CO_2 reduction activity, Chem. Eng. J. 411 (2021) 128501.

[43] X. Cui, Q. Ruan, X. Zhuo, X. Xia, J. Hu, R. Fu, Y. Li, J. Wang, H. Xu, Photothermal nanomaterials: a powerful light-to-heat converter, Chem. Rev. 123 (2023) 6891–6952.

[44] C. Song, Z. Wang, Z. Yin, D. Xiao, D. Ma, Principles and applications of photothermal catalysis, Chem. Catal. 2 (2022) 52–83.

[45] Z. Zhang, C. Mao, D. Meira, P. Duchesne, A. Tountas, Z. Li, C. Qiu, S. Tang, R. Song, X. Ding, New black indium oxide-tandem photothermal CO_2-H_2 methanol selective catalyst, Nat. Commun. 13 (2022) 1512.

[46] Y. Peng, H. Szalad, P. Nikacevic, G. Gorni, S. Goberna, L. Simonelli, J. Albero, N. López, H. García, Co-doped hydroxyapatite as photothermal catalyst for selective CO_2 hydrogenation, Appl. Catal. B: Environ. 333 (2023) 122790.

[47] X. Zhu, H. Zong, C.J.V. Pérez, H. Miao, W. Sun, Z. Yuan, S. Wang, G. Zeng, H. Xu, Z. Jiang, Supercharged CO_2 photothermal catalytic methanation: high conversion, rate, and selectivity, Angew. Chem. Int. Ed. 62 (2023) e202218694.

[48] H. Ge, Y. Kuwahara, K. Kusu, Z. Bian, H. Yamashita, Ru/H_xMoO_{3-y} with plasmonic effect for boosting photothermal catalytic CO_2 methanation, Appl. Catal. B: Environ. 317 (2022) 121734.

[49] C. Zhang, L. Wang, U. Etim, Y. Song, O. Gazit, Z. Zhong, Oxygen vacancies in Cu/TiO_2 boost strong metal-support interaction and CO_2 hydrogenation to methanol, J. Catal. 413 (2022) 284–296.

[50] P. Wang, R. Shi, Y. Zhao, Z. Li, J. Zhao, J. Zhao, G. Waterhouse, L. Wu, T. Zhang, Selective photocatalytic oxidative coupling of methane via regulating methyl intermediates over metal/ZnO nanoparticles, Angew. Chem. Int. Ed. 135 (2023) e202304301.

[51] Y. Qi, J. Jiang, X. Liang, S. Ouyang, W. Mi, S. Ning, L. Zhao, J. Ye, Fabrication of black In_2O_3 with dense oxygen vacancy through dual functional carbon doping for enhancing photothermal CO_2 hydrogenation, Adv. Funct. Mater. 31 (2021) 2100908.

[52] F. Sastre, A. Puga, L. Liu, A. Corma, H. Garcia, Complete photocatalytic reduction of CO_2 to methane by H_2 under solar light irradiation, J. Am. Chem. Soc. 136 (2014) 6798–6801.